Redox-Induced Structural Change in Anode Materials Based on Tetrahedral $(MPn_4)^{x-}$ Transition Metal Pnictides

M.-P. Bichat,[†] F. Gillot,[†] L. Monconduit,[†] F. Favier,[†] M. Morcrette,[§] F. Lemoigno,[‡] and M.-L. Doublet*,[‡]

CNRS−Laboratoire des Agrégats Métalliques et des Matériaux Inorganiques and CNRS−Laboratoire de Structure et Dynamique des Systèmes Moléculaires et Solides, Université Montpellier II, Place Eugène Bataillon, F-34 095 Montpellier Cedex 5, France, and CNRS−Laboratoire de Réactivité et Chimie des Solides, Université de Picardie Jules Vernes, 33 Rue S[t] Leu, F-80 039 Amiens Cedex 1, France

Received October 31, 2003. Revised Manuscript Received January 7, 2004

The study presents a combined experimental and computational study of Li^+ extraction/insertion mechanisms in cubic-fcc transition metal pnictides Li_xMPn_4 (MPn = TiP, VP, VAs). Exhibiting high specific capacities (C_{max} = 830 mA h g^{-1}) at a potential close to 1 V, these materials have been recently proposed as promising negative electrode materials for Li-ion battery. In situ XRD and first-principle electronic structure calculations including full structural relaxations are used to correlate the reversible structural phase transition observed in oxidation/reduction, to a loss/reconstruction of the unit cell fcc symmetry. The mechanism is rationalized in terms of a M−Pn bond contraction/elongation of the tetrahedral $(MPn_4)^{x-}$ electronic entities, on which initial structures are built. This unusual redox-induced mechanism occurs without any significant electrode volume change, thus solving one of the major drawbacks of anodes.

Introduction

In the past years, substantial research has been done to avoid carbon-related safety issues in lithium-ion batteries.[1−3] Considerable work has been devoted to metal alloy negative electrodes, such as binary Li−Al, Li−Si, and Li−Sn systems,[4−6] and to composite electrodes, such as Li_xSnO_y.[7] Exhibiting better capacities than graphite, these phases unfortunately suffer from unacceptable irreversible capacity loss or/and from important volume changes upon cycling, resulting in consequent capacity fading. Thackeray and co-workers proposed to solve these issues with intermetallic systems such as Li_xInSb. They stated that a complete InSb to Li_3Sb transition is achieved on discharge, leading to the extrusion of In^0 small particles and to Sb array expansion of less than 5%.[8,9] The small volume variation was correlated to the equivalent crystallographic structures shared by InSb and Li_3Sb: both phases crystallize in cubic structures described by antimony fcc cells, varying in volume by only 4.4%.[10] Although controversial,[11] this contribution has led to the statement that a strong structural relationship is required between the parent and lithiated electrodes, to avoid the dramatic structural damages induced by lithium insertion/extraction. Materials that combine a small volume expansion together with a wide range of lithium composition and a small molar weight are therefore highly requested in a lithium rechargeable battery field.

Following this line, we have investigated the electrochemical properties of other fcc-based pnictides, namely, the ternary Li_xMPn_4 (M = first-row transition metal; Pn = pnictogen) phases. These phases exhibit pnictide-based fcc unit cells,[12−14] same as the previously men-

* To whom correspondence should be addressed. E-mail: doublet@univ-montp2.fr.

[†] CNRS−Laboratoire des Agrégats Métalliques et des Matériaux Inorganiques, Université Montpellier II.

[‡] CNRS−Laboratoire de Structure et Dynamique des Systèmes Moléculaires et Solides, Université Montpellier II.

[§] CNRS−Laboratoire de Réactivité et Chimie des Solides, Université de Picardie Jules Vernes.

(1) Nishi, Y. In *Performance of the first lithium ion battery and its technology*; Wakihara, M., Yamamoto, O., Eds.; Lithium Ion Batteries; Kodansha: Tokyo; Wiley/VCH: Weinheim, 1998; p 181.

(2) Flandrois, S.; Simon, B. *Carbon* **1999**, *37*, 165.

(3) Yazami, R. *Electrochim. Acta* **1999**, *45*, 87.

(4) Yao, N. P.; Heredy, L. A.; Saunders: R. C. *J. Electrochem. Soc.* **1971**, *118*, 1039.

(5) Lai, S. C. *J. Electrochem. Soc.* **1976**, *123*, 1196. Sharma, R. A.; Seefurth, R. N. *J. Electrochem. Soc.* **1976**, *123*, 1763.

(6) Besenhard, J. O.; Yang, J.; Winter, M. *J. Power Sources* **1997**, *68*, 87.

(7) Idota, Y.; Matsufuji, A.; Maekawa, Y.; Miyasaki, T. *Sciences* **1997**, *276*, 1395.

(8) Vaughey, J. T.; O'Hara, J.; Thackeray, M. M. *J. Electrochem. Soc.* **2000**, *3*, 13.

(9) Johnson, C. S.; Vaughey, J. T.; Thackeray, M. M.; Sarakonsri, T.; Hackney, S. A.; Fransson, L.; Edström, K.; Thomas, J. O. *Electrochem. Commun.* **2000**, *2*, 595.

(10) Vaughey, J. T.; Johnson, C. S.; Kropf, A. J.; Benedek, R.; Thackeray, M. M.; Tostmann, H.; Sarakonsri, T.; Hackney, S.; Fransson, L.; Edström, K.; Thomas, J. O. *J. Power Sources* **2001**, *97−98*, 194.

(11) Hewitt, K. C.; Beaulieu, L. Y.; Dahn, J. R. *J. Electrochem. Soc.* **2001**, *148*, A402.

(12) Langer, K.; Juza, R. *Z. Anorg. Allg. Chem.* **1968**, *361*, 74. Juza, R.; Langer, K.; von Benda, K. *Angew. Chem., Int. Ed.* **1968**, *7*, 5.

(13) Monconduit, L.; Tillard, M.; Belin, C. *J. Solid State Chem.* **2001**, *156*, 37.

(14) Monconduit, L.; Gillot, F.; Doublet, M.-L.; Lemoigno, F. *Ionics* **2003**, *9*, 56.

10.1021/cm035101l CCC: $27.50
Published on Web 02/24/2004

tioned InSb. However, one transition metal lies in the Li_xMP_4 fcc unit cells (Pn = N, P, As) instead of four indium in the InSb fcc unit cell. This leads to more cationic sites available for lithium in MPn_4 (11 sites) than in InSb (8 sites). Hence, provided that a lithium number at least as high as that in InSb can be electrochemically extracted and reinserted from/in Li_xMPn_4, higher capacities should be achieved for the lighter Li_xMPn_4 (Pn = N, P, As). It is worth noting, however, that a complete Li^+ insertion in Li_xMPn_4 to form Li_3Pn is not here sought, as it would probably lead to electrode volume changes and poor reversibility. Indeed, the binary Li_3Pn (Pn = N, P, As) phases exhibit hexagonal crystal structures[15,16] and poor reactivity toward lithium.[17] In contrast, Li_3Sb exhibits a fcc cubic structure as well as a significant Li^+ electrochemical activity.

The electrochemical activity of various Li_xMPn_4 (M = Ti, V, Mn; Pn = N, P, As) cubic phases toward lithium has been recently investigated by several groups.[14,17−22] The results reported so far bring out common interesting features. Reports on Li^+ uptake/removal in these transition metal pnictides show lower potentials compared to those of transition metal oxides.[23,24] Rather large lithium content variation (Δx) is achieved upon charge and discharge. It reaches up to 10 depending on M and Pn and leads to good initial gravimetric capacities. Generally, nitrides show lower weighted capacities than phosphides and arsenides. Hence, Li_7MnN_4,[20,21] Li_7MnP_4,[22] and Li_9VAs_4[14] exhibit capacities of 310, 700, and 685 mA·h/g, respectively. To explain these differences, it is essential to obtain more insight into the lithium extraction/insertion mechanisms in these materials. Of particular concern is to figure out how crystal and electronic structures may accommodate such large variations of Li^+ and electrons (per unit cell).

Until now, very little has been done to address this question. Nazar and co-workers have proposed a quasi-topotactic intercalation mechanism when lithium is inserted into the monoclinic binary MnP_4, to form the cubic ternary Li_7MnP_4.[22] During the process, P−P bonds in the binary layered phosphide are first cleaved to form the crystalline Li_7MnP_4 phase and then reformed in charge when MnP_4 is re-crystallized. However, a significant capacity loss is observed during the first charge: the potential/composition curve presented by the authors shows that the initial electrode composition is not recovered at the end of charge. If, as stated by the authors, a complete MnP_4 reconstruction is achieved during charge, what is therefore the origin of the capacity loss? More recently, a different structural behavior has been reported by Palacin et al. for Li_7MnN_4 as well as for analogous oxonitrides $Li_7MnN_{4-y}O_y$.[20] In these systems, no more than 2.2 Li^+ are reversibly extracted from the starting high-lithiated electrodes, and in situ X-ray diffraction (XRD) patterns show a progressive electrode amorphization upon cycling. However, no interpretation was given about the mechanism responsible for the amorphous phase formation. In a recent work on Li_xVPn_4 (Pn = P, As), we proposed a mechanism involving the tetrahedral $(MPn_4)^{x-}$ anions[18] as the main redox center to explain the promising electrochemical properties of these materials. On the basis of first-principle electronic structure calculations, this mechanism assumes that both low-lithiated and high-lithiated phases consist of stable $(MPn_4)^{x-}$ electronic entities, with an anionic charge directly correlated to the lithium composition x. In this work, however, neither in situ XRD nor structural relaxations were performed to confirm this hypothesis. Thus, the questions of Li^+ extraction/insertion mechanisms, and induced electrode volume changes upon cycling remain to be addressed.

This is the aim of the present work, to elucidate Li^+ electrochemical insertion mechanisms in ternary transition metal pnictides and to obtain deeper insight into their structural behavior upon cycling. To reach that goal, single-phase Li_9TiP_4 and Li_9VAs_4 electrodes were first prepared using two different synthetic routes, as previously reported.[13,14,19] Furthermore, galvanostatic and potentiodynamic measurements, in situ XRD upon cycling, and first-principle structure relaxations were carried out. The paper is organized as follows: the next section briefly reviews the electrode synthesis and characterization. Experimental (section II) as well as computational (section III) details and results are then given for Li_9TiP_4 and Li_9VAs_4 single phases and compared to previous galvanostatic measurements reported for Li_7VP_4.[18] This latter phase, which could not be obtained as a single phase, is presented here as a comparative study. Structural and electrochemical behaviors are discussed in the last section where an original mechanism is proposed to explain the different charge and discharge processes.

1. Background

1.1. Pristine Compounds Preparation and Characterization. Li_9MPn_4 (MPn = TiP, VP, VAs) phases were first prepared from stoichiometric proportions through high-temperature ceramic routes. Elements were placed inside metal (Nb or Ta) or stainless steel tubes sealed under argon by arc welding, in the thermal conditions described in a previous work.[13,14] Air- and moisture-sensitive starting materials and products were handled in an argon-filled glovebox. Reaction products were characterized using XRD patterns and recorded on an X-Pert Philips diffractometer, with monochromatic Cu $K\alpha_1$ as the radiation source. While Li_9VAs_4 was obtained as a single phase,[14] every phosphide-based reaction product was contaminated by binary phases, such as Li_3P and MP_y. To prevent the formation of such impurities, ball-milling synthesis was successfully developed as an alternative method.[19] The method uses a

(15) Calvert, L. ICDD Grant-in-Aid, National Research Council of Canada: Ottawa, Canada, 1978; PCPDF 30-0759.
(16) Brauer, J.; Zintl, Z. *Phys. Chem.* **1937**, *37*, 323; PCPDF 04-0502.
(17) Gillot, F.; Bichat, M.-P.; Favier, F.; Morcrette, M.; Doublet, M.-L.; Monconduit, L. *Electrochim. Acta* **2004**, in press. Gillot, F. Ph.D. Thesis, Universite Montpellier II, 2003. Gillot, F.; Bichat, M.-P.; Favier, F.; Morcrette, M.; Tarascon, J.-M.; Monconduit, L. *Ionics* **2003**, *9*, 71−76.
(18) Doublet, M.-L.; Lemoigno, F.; Gillot, F.; Monconduit, L. *Chem. Mater.* **2002**, *14*, 4126.
(19) Morcrette, M.; Gillot, F.; Monconduit, L.; Tarascon, J.-M. *Electrochem. Solid State Lett.* **2003**, *6*, A59.
(20) Cabana, J.; Rousse, G.; Fuertes, A.; Palacin, M. R. *J. Mater. Chem.* **2003**, *13*, 2402.
(21) Suzuki, S.; Shodai, T. *Solid State Ionics* **1999**, *116*, 1.
(22) Souza, D. C. S.; Pralong, V.; Jacobson, A. J.; Nazar, L. F. *Science* **2002**, *296*, 2012.
(23) Armstrong, A. R.; Bruce, P. G. *Nature*, **1996**, *381*, 499.
(24) Whittingham, M. S. *J. Electrochem. Soc.* **1975**, *123*, 315.

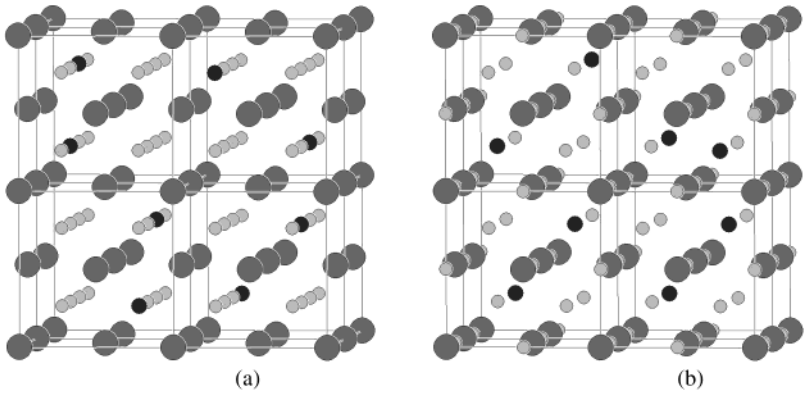

Figure 1. Li_7MPn_4 2 × 2 × 2 super-cells described within (a) $Fm\bar{3}m$ and (b) $F\bar{4}3m$ space groups. Black, gray, and light-gray circles correspond to M, Pn, and Li atoms, respectively.

Table 1. Unit Cell Parameters *a* (Å), Scan Rates, Number of Extracted/Inserted Li^+ (Δx), and Specific Capacities (mA·h/g) for Li_9TiP_4 and Li_9VAs_4 Single Electrodes and for Li−V−P Electrode; BM and HT Refer to Ball-milling and High-Temperature Synthesis

Li_xMPn_4	$a = b = c$ (Å)	scan rate (1Li/*n*h)	Δx_{ox}	Δx_{red}	specific capacity (mA·h/g)
Li_9TiP_4 single-phase BM	6.01 (1)	1Li/2h	6.1	7.4	830
Li_9VAs_4 single-phase HT	6.16 (1)	1Li/10h	6.8	8.6	582
Li−V−P_4 HT	5.995 (4)	1Li/20h	4.0	4.6	550

Spex 8000 mixer-mill that generates mechanical strain. Amounts of required precursor raw powders (M, Pn, and Li elements loaded in a glovebox) were placed into a stainless steel container together with steel balls. Weight ratio of steel balls to powder as well as sample grinding time were taken from a previous work.[19] Grinding vial loading and sealing were done in a glovebox. As prepared powders were then annealed (50 °C/h) for a week, in sealed stainless steel containers, and kept at 500 and 900 °C before being promptly quenched (liquid air). Applied to various Li_xMP_4 (M = Ti, V) stoichiometries, the method has successfully led to nicely crystallized Li_9TiP_4 samples devoid of any impurity phases. For the vanadium phosphide, significant amounts of binary impurities were found in the reaction products, thus avoiding any accurate $Li_xV_yP_4$ stoichiometry determination. Thus, data for this latter system (hereafter referred to as Li−V−P) will be considered as indicative and qualitative results.

1.2. Structural Description. The literature describes ternary Li_xMPn_4 phases (Figure 1 for $x = 7$) either in the centro-symmetric $Fm\bar{3}m$ (No. 225) space group or in the non-centro-symmetric $F\bar{4}3m$ (No. 216) one.[12,13] In both structures, pnictogen atoms lie on the 4-folded 4a (0,0,0) crystallographic positions with the $m\bar{3}m$ and $\bar{4}3m$ symmetries, respectively. They form a fcc unit cell in which 12 (4 octahedral and 8 tetrahedral) Pn-coordinated cationic vacancies are available. Depending on both the lithium composition and the cationic distribution, such as ordering in tetrahedral sites for M and Li, cells adopt either the $Fm\bar{3}m$ symmetry or the $F\bar{4}3m$ symmetry.

2. Experimental Section

2.1. Electrochemical Measurements and in Situ XRD. Though the Li_xMPn_4 are candidates for negative battery electrodes, we have used a system for studying their properties in which the Li_xMPn_4 electrode is the positive electrode. Electrochemical tests for Li^+ extraction/insertion were performed in Swagelok-type cells, assembled in an argon-filled drybox, with oxygen and water contents below 5 ppm. Cells consist of a composite electrode containing 10−12 mg of active material mixed with 15% of acetylene black, a Li-metal disk, as the negative electrode, and a Whattman-GF/D borosilicate glass micro-fiber separator, saturated with a 1 M $LiPF_6$ (EC:DMC, 1:1) electrolyte solution (Merck S.A) and placed between the two electrodes. Electrochemical extraction/insertion was monitored using an automatic

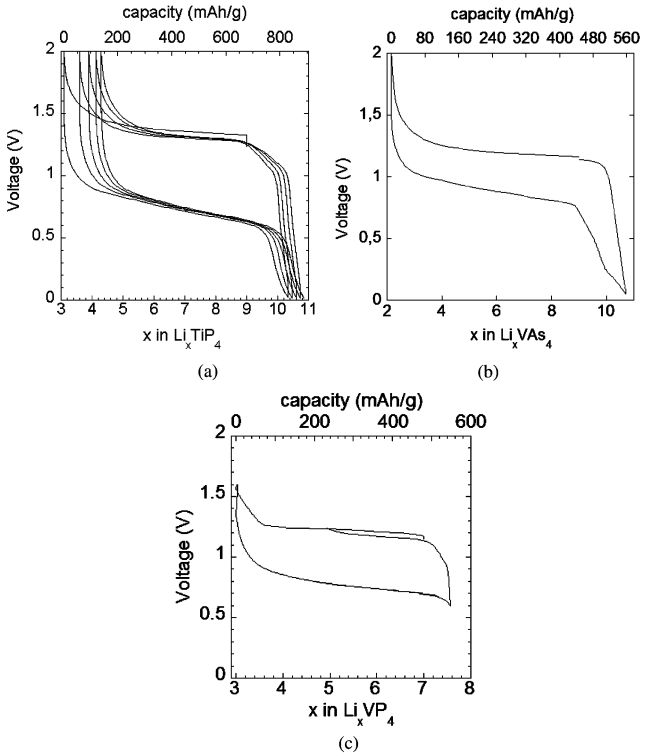

Figure 2. Potential vs composition curves started in charge for (a) Li_9TiP_4/Li, (b) Li_9VAs_4/Li, and (c) Li−V−P/Li cells. Scan rates and capacities are listed in Table 1.

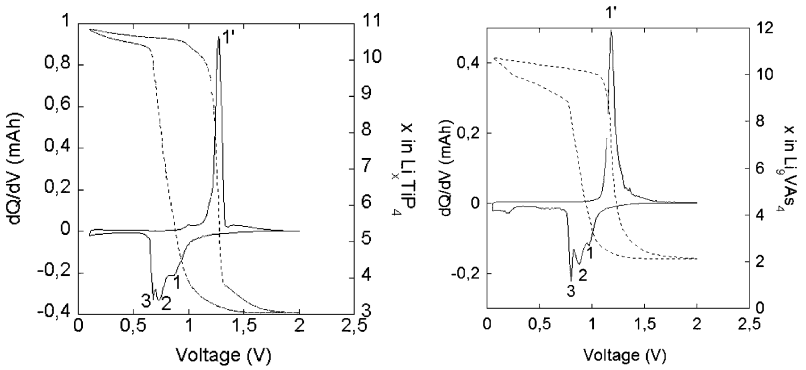

Figure 3. Potentiodynamic cycling with galvanostatic at an equivalent current of 1Li/10h for (a) Li_9TiP_4/Li and (b) Li_9VAs_4/Li cells.

cycling data recording system (Mac-Pile Biologic SA, Claix, France) and operating in galvanostatic, GITT (galvanostatic intermittent titration technique) or PITT (potentiostatic intermittent titration technique), modes in the range from 2 to 0.02 V.

To point out any structural modification induced by Li^+ extraction/insertion, in situ X-ray experiments were performed on cycling Li/Li_9MPn_4 cells, using a D8 Brucker X-ray diffractometer with monochromatic Co $K\alpha_1$ or Cu $K\alpha_1$ as radiation sources. The in situ XRD technique has already proved to be a powerful tool to study battery electrode materials.[2525] Electrochemical cells were assembled in a drybox using a modified Swagelok cell as described in ref 17. The electrode material is sampled underneath a berrylium window used as a current collector. The complete device is then placed in the diffractometer and connected to the Mac-Pile, operating in the GITT mode.

2.2. Electrochemical Results. Galvanostatic measurements were started in oxidation from the crystallized Li_9VAs_4 and Li_9TiP_4 single-phase electrodes. Equivalent conditions were applied to the Li−V−P electrode. Rather low scan rates were used to approach full capacities. Unit cell parameters, scan rates, total number of exchanged Li^+ during the first cycle (Δx_{ox}, Δx_{red}), and corresponding specific capacities are listed in Table 1.

Both single-phase electrodes exhibit high capacities of 830 mA·h/g for Li_9TiP_4 and 582 mA·h/g for Li_9VAs_4, correlated with large lithium content variations (Δx_{red} = 7.4 for Li_9TiP_4 and 8.6 for Li_9VAs_4). Note that the highest lithium composition achieved by electrochemical insertion ($x \sim 11$) corresponds to a complete filling of every cationic vacancy available in the unit cells. For Li−V−P, the capacity has been estimated to 550 mA·h/g.

Equivalent electrochemical behaviors are observed for the three electrodes. The voltage versus composition curves obtained for Li_9TiP_4, Li−V−P, and Li_9VAs_4 are given in Figure 2. They show a well-defined plateau in oxidation at 1.30 V for Li_9TiP_4, 1.20 V for Li−V−P, and 1.19 V for Li_9VAs_4. In reduction, different processes are observed, correlated with different slopes in the potential curves. The first observation that comes to mind is the difference between oxidation and reduction. One can also notice that such a difference remains upon cycling, as shown in Figure 2a for Li_9TiP_4.

In oxidation, the very flat plateau is the signature for a two-phase process. This is confirmed by a sharp peak of incremental capacity (Figure 3) and by the shape of the current, under PITT mode (Figure 4). The latter curve emphasizes that the electrocrystallographic transformation follows a bell shape in oxidation (process **1′**). As shown in the insert **1′** of Figure 4a,b, a flat time dependence of current is observed when the potential reaches the plateau value. This indicates that the front phase migration is the process-limiting step.[26,27] As shown in XRD patterns, Figure 5, the characteristic peaks of the fcc initial structures progressively disappear as Li^+ is extracted from the crystallized Li_9TiP_4 and Li_9VAs_4 electrodes. In contrast to the results previously reported for Li_7MnP_4,[22] there is no evidence for any monoclinic MPn_4 phase growing in the electrode during charge. The two-phase process in oxidation thus corresponds to a complete structural phase transition from the crystalline starting phase to an X-ray amorphous phase.

In reduction, three distinct peaks of incremental capacity are observed for both Li_9TiP_4 and Li_9VAs_4 (Figure 3). A more complex mechanism is thus achieved in reduction, probably correlated to different ionic or/and electronic regimes. The two first peaks associated with processes **1** and **2** are broad, suggesting two successive single-phase processes. As shown by inserts **1** and **2** of Figure 4a,b, however, the current decay for these two processes does not fit exactly the Fick law that one may expect for a classical single-phase process. Work is in progress to elucidate that specific point. The third peak associated with the lowest potential (0.69 V for Li_9TiP_4 and 0.80 V for Li_9VAs_4) is clearly sharper than the two previous ones, suggesting a two-phase process at the end of reduction. This is confirmed by a flat time dependence of current, at these potentials (insert **3** of Figure 4a,b). Meanwhile, in situ X-ray patterns show the reappearance of the initial fcc characteristic peaks at the end of discharge (Figure 5). Even if a peak broadening is observed for the discharged

(25) Morcrette, M.; Chabre, Y.; Vaughan, G.; Amatucci, G.; Leriche, J.-B.; Patoux, S.; Masquelier, C.; Tarascon, J.-M. *Electrochim. Acta* **2002**, *47*, 3137.

(26) Chabre, Y. In *Chemical Physics of Intercalation*; Bernier, P., et al., Eds.; Plenum: New York, 1993.

(27) For technical information about such specific experiments, see: Patoux, S.; Masquelier, C. *Chem. Mater.* **2002**, *14*, 2334.

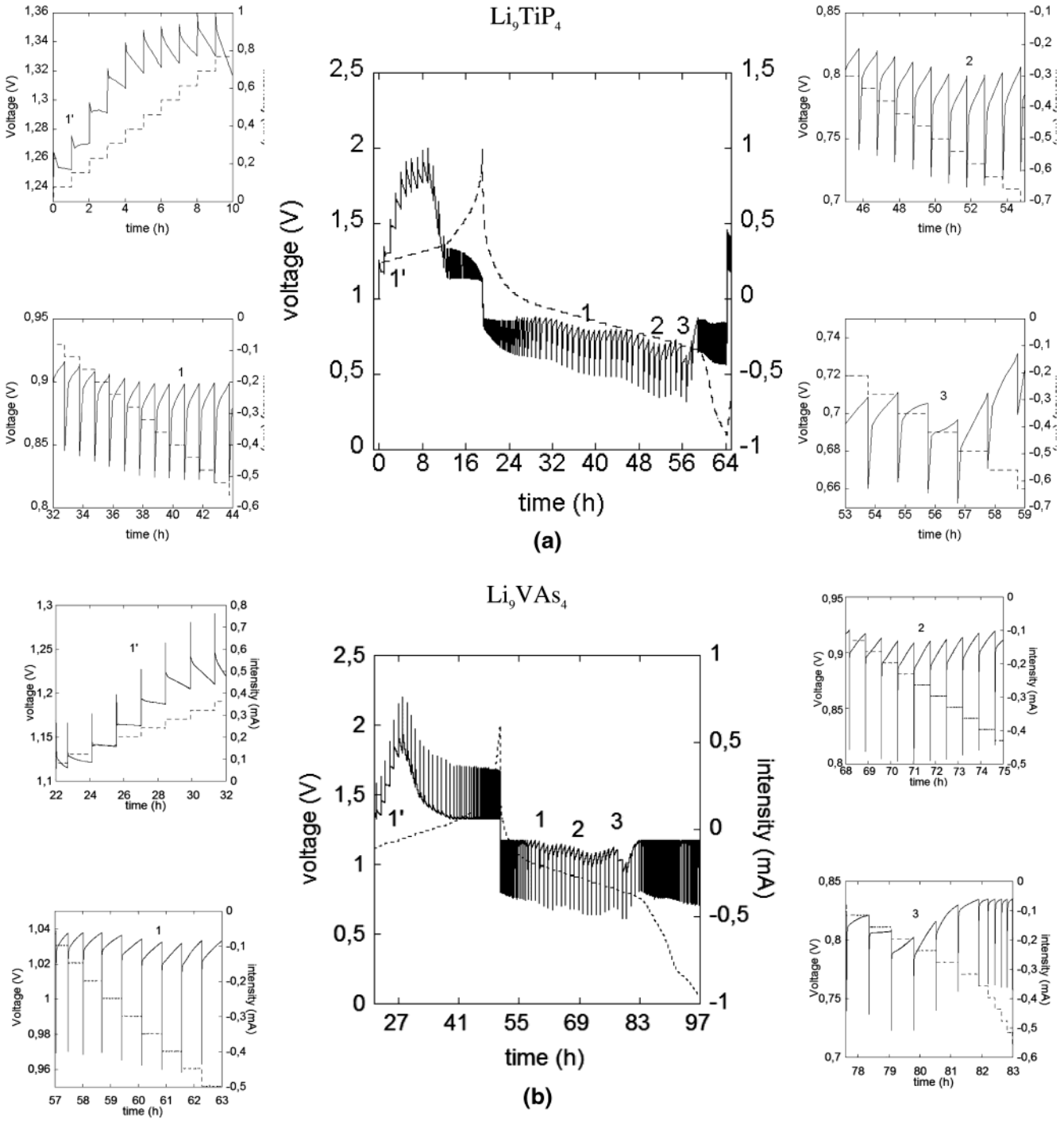

Figure 4. Current decay as a function of time measured in PITT mode for (a) Li_9TiP_4/Li and (b) Li_9VAs_4/Li cells. Inserts correspond to the process in oxidation (**1′**) and the three processes in reduction (**1**, **2**, **3**). Experiments have been done through potential increments of 10 mV. Voltage changes occur when the absolute current reaches a value corresponding to a C/100 scan rate.

electrodes compared to that of the initial ones (likely due to an imperfect recovery of the long-range order or/and a decrease of the particle size), most of the initial peak surface is recovered at the end of discharge (Figure 6). This indicates that a (nearly) complete and reversible phase transition is induced by Li^+ redox chemistry in Li_9MPn_4 (MPn = TiP, VAs). Note that slight changes in relative intensities are also observed for Li_9VAs_4 between starting and discharged electrodes. This could be due to different cationic distributions.

The above results demonstrate a low-potential electrochemical reactivity of Li_9TiP_4, Li−V−P, and Li_9VAs_4 toward elemental lithium. Up to 9 Li^+ are exchanged during a complete charge and discharge cycle, through similar electrochemical and structural mechanisms (at least for the two single-phase electrodes). Such large lithium content variations obviously exclude a mechanism involving transition metal redox reactions. Actually, we aim at showing that redox chemistry in transition metal pnictides involves stable $(MPn_4)^{x-}$ anionic entities, able to accommodate large charge variations without drastic structural change. This analysis will allow us to understand the reversible fcc loss/reconstruction mechanism as an unusual solid-state

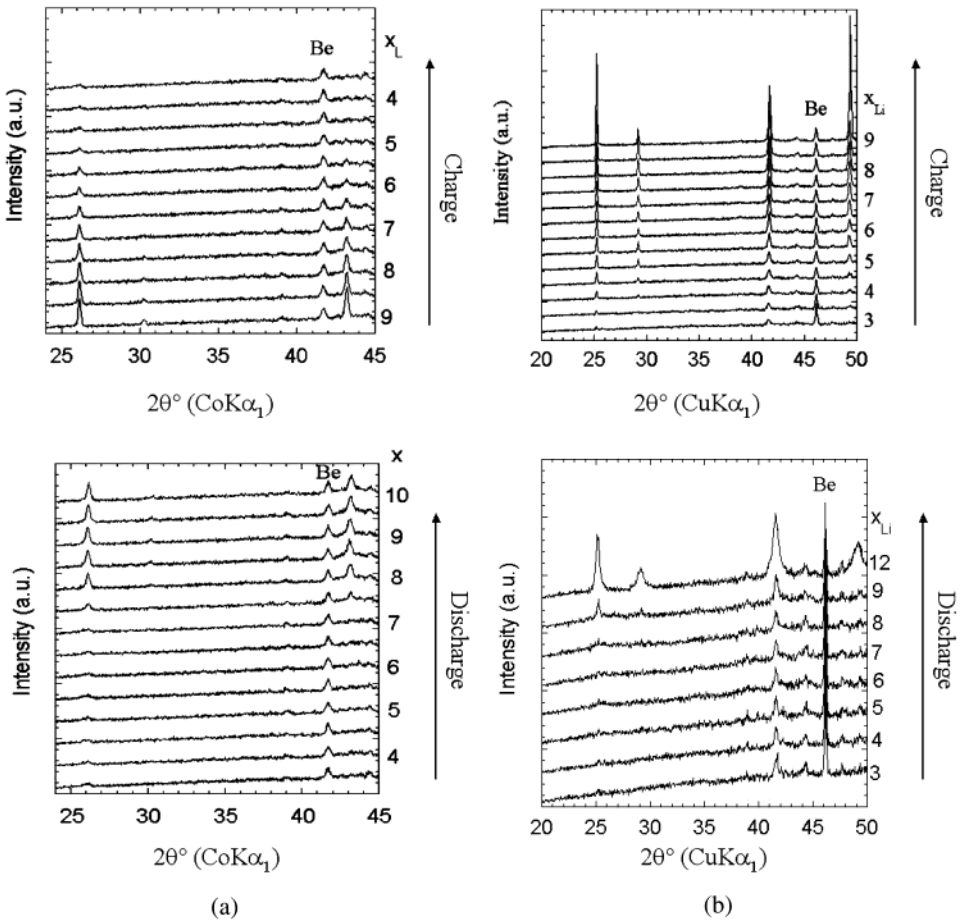

Figure 5. In situ XRD for the first charge (up) and discharge (down) sweeps for (a) Li_9TiP_4/Li and (b) Li_9VAs_4/Li cells.

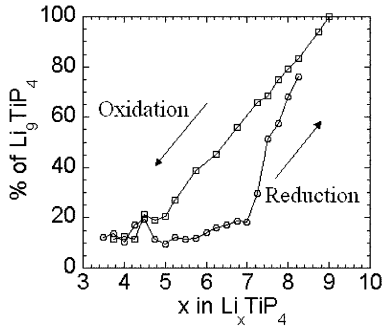

Figure 6. Peak surface integration for the $Fm\bar{3}m$ most intense peak upon the first charge and the first discharge.

crystalline transition which prevents electrode volume changes.

3. Electronic Structure Calculations

3.1. Computational Details and Method. In an attempt to explain experiments, first-principle electronic structure calculations and structural relaxations were performed, using three different codes based on the density functional theory (DFT) formalism. The ADF-Band program package of Baerends et al.[28] utilizes Slater-type orbitals and numerical orbitals as the initial basis set and was used to perform local chemical bond analysis. For a better treatment of M−Pn electronic repulsions, the gradient-corrected functional of Perdew-Wang[29] was chosen for the exchange-correlation energy. Density of states (DOS) as well as crystal orbital overlap populations (COOP) for the M−Pn and Pn−Pn bonds were calculated. The latter display the bonding (COOP > 0), nonbonding (COOP ~ 0), and antibonding (COOP < 0) character of one given local bond in the whole range of energy. To provide a clearer picture of the results, electron density plots were computed using the full-potential linearized augmented plane waves (FLAPW) code WIEN97.[30] The generalized gradient approximation (GGA)[31] was used for every calculation with a plane waves basis set, up to 600 eV, to reach the convergence of calculations. To check any possible structural modifications induced by the electrochemical redox reactions, full structural relaxations for different lithium compositions and/or distributions were investigated using the VASP (Vienna Ab Initio Simulation Package) code of Haffner et al.[32] Convergence of calculations was checked with respect to both the *k*-points grid (up to $10 \times 10 \times 10$ Monkhorst-Pac mesh) and the plane waves energy cutoff (up to 600 eV) in the generalized gradient approximation (GGA).

(28) Te Velde, G. Ph.D. Thesis, Vrije Universiteit, Amsterdam, 1990. Te Velde, G.; Baerends, E.-J. *Phys. Rev. B* **1991**, *44*, 7888.

(29) Perdew, J.-P.; Wang, Y. *Phys. Rev. B* **1992**, *45*, 244.

(30) Blaha, P.; Schwarz, K.; Luitz, J. *WIEN97: A full potential linearized augmented plane wave package for calculating crystal properties*; Karlheinz Schwarz, Techn. Universität Wien, Austria, 1999; ISBN 3-9501031-0-4 (An improved version: Blaha, P.; Schwarz, K.;. Sorantin, P.; Trickey, S. B. *Comput. Phys. Commun.* **1990**, *59*, 399).

(31) Perdew, J.-P.; Burke, S.; Ernzerhof, M. *Phys. Rev. Lett.* **1996**, *77*, 3865.

(32) Kresse, G.; Hafner, J. *Phys. Rev. B* **1993**, *47*, 558.

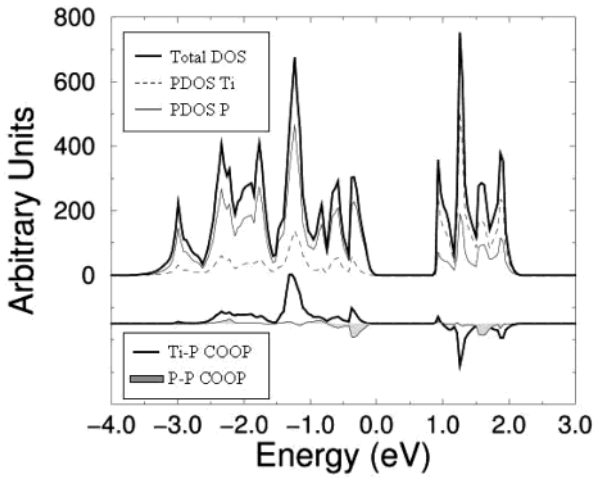

Figure 7. Density of states (DOS) and crystal orbital overlap population (COOP) plots for Li_8TiP_4. Ti−P and P−P COOPs are represented by solid and filled lines, respectively. Zero energy corresponds to the Fermi level.

3.2. Electronic Structure of $Li_{(2n-3)}M^{n+}Pn_{(n-1)}$ Phases. From a formal electron count, charge equilibration in Li_xMPn_4 phases leads to different cationic compositions depending on the transition metal oxidation state, that is, $Li_5Ti^{IV}P_3$ (=$Li_{6.666}Ti_{1.333}P_4$) and $Li_7V^{V}Pn_4$ (Pn = P, As). Hence, either more than one transition metal or more than seven lithiums are required in Ti-based systems to reach equivalent fcc formal charge, that is, $(Pn^{3-})_4$. To make easy the comparison with Li_7VPn_4 (Pn = P, As), Li_8TiP_4 was chosen. The DOS and COOP calculated for Li_8TiP_4, using the unit cell parameter refined for Li_9TiP_4 (a = 6.01 (1) Å), are presented in Figure 7. They are very similar to those already reported for Li_7VP_4 and Li_7VAs_4.[18] As for Li_7VPn_4 (Pn = P, As), the Li_8TiP_4 lattice describes a network of weakly interacting (TiP_4) tetrahedra doped by localized Li^+ cations, rather than a Pn-fcc bulk doped by Ti^{4+} and Li^+ cations. A crystal orbital analysis reveals that the low-lying filled band and the high-lying empty band are built on local (TiP_4) bonding and antibonding molecular levels, respectively. Consequently, P−P COOPs are much smaller in magnitude than Ti−P COOPs in the whole range of energy. This means that electron density is mainly located along Ti−P bonds rather than between tetrahedra. The addition (removal) of extra electrons to (from) the system will thus affect both transition metal and pnictogen electronic populations.[33] Redox chemistry in these compounds thus involves $(MPn_4)^{x-}$ electronic entities instead of M^{n+} cations. This description is supported by electron density plots. As depicted in Figure 8a, the valence density is strongly polarized inside the tetrahedral transition metal coordination sphere, while it is much weaker between pnictogen atoms belonging to different tetrahedra. Regarding the electrochemical activity, such an electron density shape should favor lithium insertion and diffusivity, as it results in wide charge vacancy between tetrahedra.

3.3. Structural Relaxations of Li_xMPn_4 (x = 3−11; MPn = TiP, VP, VAs). To follow the structural changes induced by Li^+ extraction/insertion, full ionic relaxations were investigated for Li_xTiP_4, Li_xVP_4, and Li_xVAs_4, for various lithium compositions starting from x = 3−11 (x = 3 is the lowest composition allowing a comparison between every Li_xMPn_4 system). This composition range leads to 32 different cationic distributions $Li(Oh)_nLi(Td)_mMPn_4$, depending on the octahedral and/or tetrahedral occupation number associated with one given composition ($x = n + m$). Among those (n,m) cationic composition/distributions, (0,3), (4,3), (0,7), and (4,7) show the highest symmetries. The first one corresponds to the blende-type structure ($F\bar{4}3m$), with half the tetrahedral sites filled (4c or 4d sites). The second structure is equivalent to the first one, with all octahedral (4b) sites occupied, as well. The third and fourth distributions correspond to the antifluorite-type structure ($Fm\bar{3}m$) and the completely filled structure, respectively.

Each of those key compositions/distributions were chosen to study the influence of cationic filling on Li_xMPn_4 crystal structures, although they correspond to a slightly different formal electron count in Li_xTiP_4 compared to that in Li_xVPn_4 (Pn = P, As). The less symmetrical (2,7) composition/distribution was also investigated for comparison with experiments. For x = 7, two different lithium distributions were studied to check which of the $Fm\bar{3}m$ or $F\bar{4}3m$ symmetries is thermodynamically favored. Note that, from electrostatic considerations, the former should be preferred to the latter, as far as equivalent unit cells are considered. For every (n,m) composition/distribution, except (2,7), single-cell calculations were performed. For (2,7), 2 × 2 × 2 super-cell was preferred to account for the partial and statistical occupation of octahedral sites. Full structural relaxations of both unit cell parameters and atomic internal coordinates were investigated in the $P1$ space group to avoid any symmetry constraint. The cell parameters previously refined for Li_9TiP_4,[19] Li−V−P,[17] and Li_9VAs_4[14] were used as starting points for ionic relaxations.

Results are presented in Table 2, with the unit cell parameter (a), the M−Pn distance, and the total cohesive energy listed for each relaxed Li_xMPn_4. Note that whatever the relaxed system, the unit cell keeps its cubic symmetry, that is, $a = b = c$ (within $\Delta a = 10^{-3}$ Å) and $\alpha = \beta = \gamma = 90°$ (within $\Delta\alpha = 10^{-2}$ degrees) and the transition metal keeps its initial crystallographic position ($^1/_4$ $^1/_4$ $^1/_4$) as well as its initial tetrahedral environment (4 equivalent M−Pn distances and unchanged angles).

From x = 3 to x = 7. The first remarkable point is that a does not show a linear dependency on lithium composition. Calculations show that x is directly correlated to the M−Pn bond distance, while the number of tetrahedral lithiums mainly influences the unit cell parameter, and therefore the unit cell volume. Compared to $Li_0^{Oh}Li_3^{Td}MPn_4$ systems, $Li_4^{Oh}Li_3^{Td}MPn_4$ systems show a significant increase of M−Pn bond lengths, in size-equivalent unit cells. For a given composition but different distributions, namely, $Li_4^{Oh}Li_3^{Td}MPn_4$ and $Li_0^{Oh}Li_7^{Td}MPn_4$, equivalent M−Pn bond lengths are obtained in size-different unit cells. As expected, $Li_0^{Oh}Li_7^{Td}MPn_4$ structures are energetically preferred to $Li_4^{Oh}Li_3^{Td}MPn_4$ structures, by at least 2 eV. A

(33) A detailed analysis of V and Pn (Pn = P, As) net populations is provided in ref 18 for Li_3VPn_4 and Li_7VPn_4 systems.

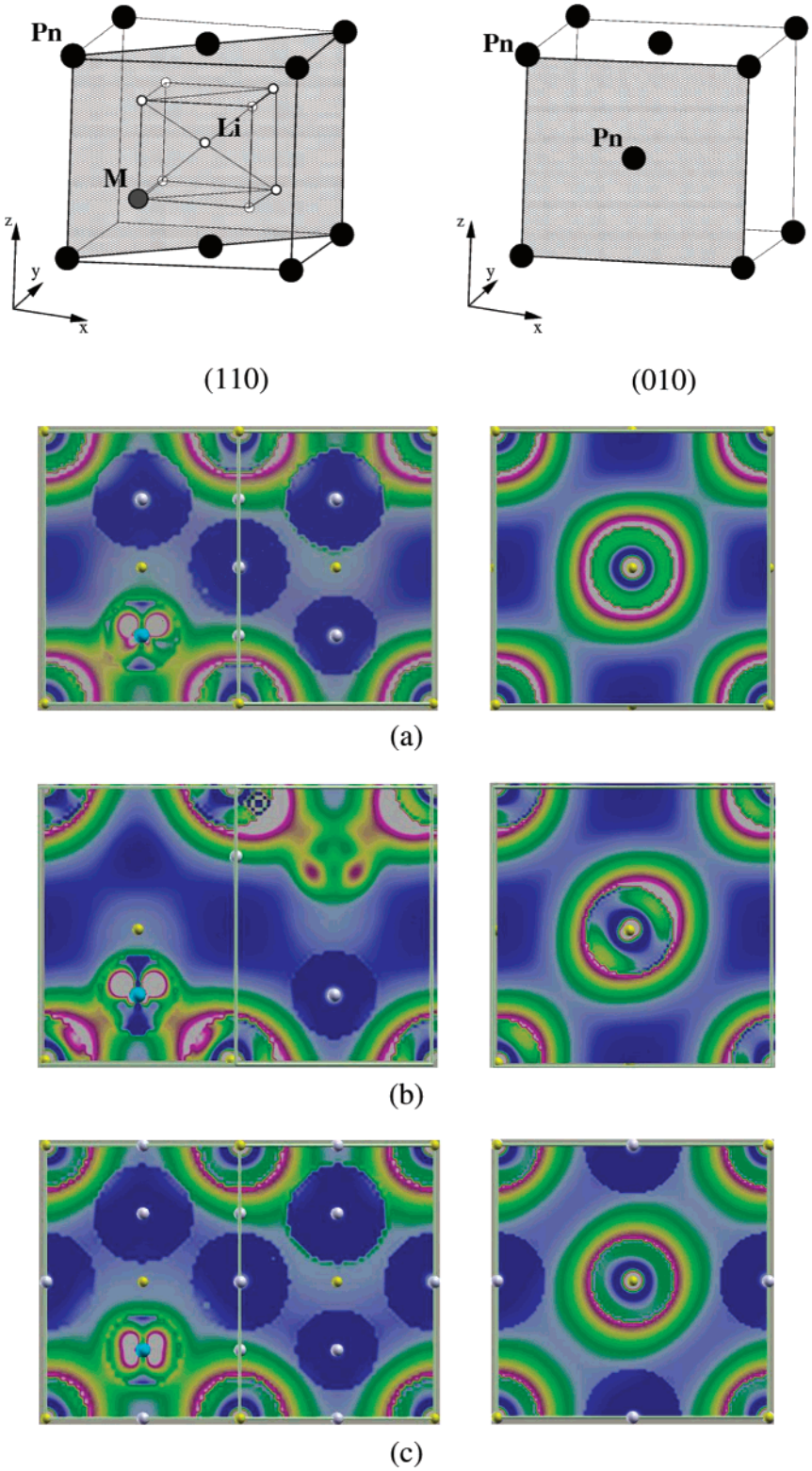

Figure 8. Electron density plots for (a) relaxed Li_8TiP_4, (b) relaxed Li_3TiP_4, and (c) relaxed $Li_{11}TiP_4$ structures. For each system, electron density from 0.013 to 0.3 electron/Å^3 is projected on the (110) and (010) planes, illustrated on the top part of the figure.

surprising result, however, is that no univocal relaxed structure is obtained for $x = 7$, although both distributions (4,3) and (0,7) correspond to wells in the potential energy surface. This means that Li^+ diffusion from one site (Oh) to another (Td) likely involves large energetic barriers and suggests that electrochemical processes should be limited by the kinetics. Since equivalent (MPn_4) tetrahedra occur in the relaxed $Li_4^{Oh}Li_3^{Td}MPn_4$ and $Li_0^{Oh}Li_7^{Td}MPn_4$ structures, electrostatic interactions might be primarily responsible for the two distributions energy difference. Li^+ electrochemical insertion in tetrahedral sites is therefore expected from $x = 3$ to $x = 7$, provided that thermodynamical equilibrium is achieved during the discharge.

Special attention should now be given to M−Pn bond lengths. Compared to *a*, they show larger relative

Table 2. Unit Cell Parameters *a* (Å), M−Pn Bond Lengths (Å), and Total Cohesive Energies (eV) Obtained from Structural Relaxations for Li_xTiP_4, Li_xVP_4, and Li_xVAs_4 (x = 3, 7, 9, 11)[a]

$Li_n^{Oh}Li_m^{Td}MPn_4$ (n,m) $x = n + m$		(0,3) 3	(4,3) 7	(0,7) 7	(2,7) 9	(4,7) 11
Li_xTiP_4	$a = b = c$ (Å)	5.69	5.71	5.82	5.88 (6.01)	5.91
	Ti−P (Å)	2.33	2.37	2.38	2.52 *(2.60)*	2.56
	energy (eV)	−33.61	−48.97	−51.70	−56.96	−59.89
Li_xVP_4	$a = b = c$ (Å)	5.65	5.65	5.74	5.80 (5.97)	5.85
	V−P (Å)	2.20	2.29	2.30	2.42 (2.58)	2.51
	energy (eV)	−35.37	−49.93	−52.64	−56.86	−60.21
Li_xVAs_4	$a = b = c$ (Å)	5.84	5.85	5.94	6.01 (6.15)	6.06
	V−As (Å)	2.29	2.38	2.39	2.56 (2.66)	2.61
	energy (eV)	−33.04	−47.08	−48.44	−53.74	−57.31

[a] Labels (n,m) correspond to the octahedral (n) and tetrahedral (m) sites occupation numbers. Values in parentheses correspond to experimental data.

variations (about 5% when x increases from 3 to 7), indicating that M−Pn bonds are much more x sensitive than unit cell volumes. This result is consistent with DOS and COOP analyses, showing that electron density is mainly located along the M−Pn bonds. It can be understood by means of electrostatic interactions as well. To compensate the lack of cationic charges induced by the removal of Li^+, $(MPn_4)^{x-}$ densities seek to become less diffuse. An (MPn_4) contraction is thus induced by a partial re-localization of the electron density along the M−Pn bonds when electrons (respectively Li^+) are progressively removed from the low-lying band (respectively electrode). This is illustrated by a P valence density much more polarized inside the tetrahedral coordination sphere for Li_3TiP_4 (Figure 8b) than for Li_8TiP_4 (Figure 8a).

These theoretical results have remarkable consequences on both Li_xMPn_4 unit cell volume and local symmetry. First, small volume expansion is expected when cationic sites are filled with Li^+ from $x = 3$ to $x = 7$. Whatever the cationic filling considered, the unit cell parameter variation is limited to 0.1 Å ($\Delta a/a \leq 2\%$) in this composition range. Second, none of the relaxed Li_xMPn_4 phases from $x = 3$ to $x = 7$ shows a fcc local symmetry. To illustrate the latter point, let us focus on the two-dimensional representation of a $2 \times 2 \times 2$ fcc super-cell given Figure 9a. In this picture, the dotted lines show some of the fcc diffraction planes. In such a symmetric cell, each Pn atom is surrounded by 12 Pn next-nearest neighbors at $d_{PnPn} = a\sqrt{2}/2$ and four equivalent M−Pn bonds are found at $d_{MPn} = a\sqrt{3}/4$. For each relaxed Li_xMPn_4 phases from $x = 3$ to $x = 7$, the M−Pn bond contraction occurring simultaneously with a smaller contraction of the a parameter leads to M−Pn bond lengths significantly smaller than $a\sqrt{3}/4$. This (even slight) structural modification is sufficient to move the four Pn atoms away from their initial crystallographic positions, inducing a destruction of the fcc diffraction planes (Figure 9b). Low-lithiated phases thus correspond to Pn-disordered lattices. It is worth noting, that a fingerprint of the initial long-range cubic order is kept, however, in each relaxed structure from $x = 3$ to $x = 7$. This cubic order is dictated by the center of mass of each (MPn_4) tetrahedron (i.e., the transition metal), which remains in its initial position, whatever the lithium composition and/or distribution considered in our calculations. From $x = 3$ to $x = 7$, Li_xMPn_4 relaxed structures can therefore be described in cubic lattices with an x-dependent unit cell parameter $a(x)$. In each unit cell, Pn atoms are fully disordered and M is statistically distributed over eight sites that would correspond to the 8c positions in the $Fm\bar{3}m$ symmetry.

From $x = 7$ to $x = 11$. Compared to the first electronic regime ($x \leq 7$), the band involved in electron transfers from $x = 7$ to $x = 11$ is now the high-lying band built on M−Pn antibonding levels and weakly antibonding Pn−Pn levels. A M−Pn bond elongation thus occurs simultaneously with a smaller increase of the a parameter (see Table 2). The addition of four Li^+ from $x = 7$ to $x = 11$ yields a $\Delta a/a$ variation of ~2%. In contrast to lower lithium compositions, high-lithiated relaxed structures (Li_9MPn_4 or $Li_{11}MPn_4$) show M−Pn distances that (almost or exactly) fit the $a\sqrt{3}/4$ value expected for fcc cells in which M lies at ($^1/_4$ $^1/_4$ $^1/_4$). Note that a better agreement with experiments is obtained for the relaxed

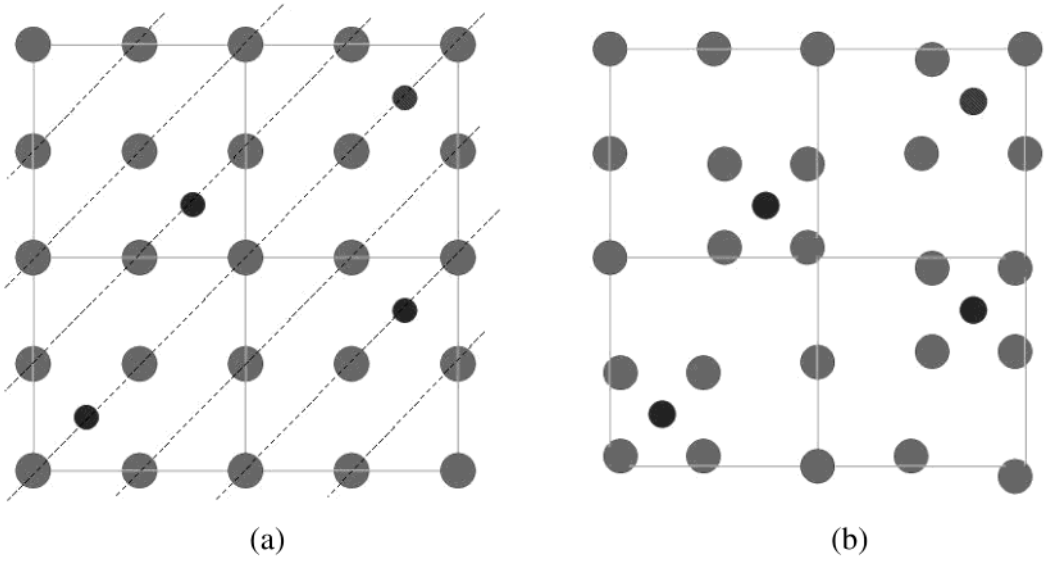

Figure 9. Two-dimensional representation of (a) an ideal $2 \times 2 \times 2$ Pn-fcc super-cell in which M is statistically distributed over the 8c ($^1/_4$ $^1/_4$ $^1/_4$) positions. Dotted lines stand for some of the Pn diffraction planes. (b) $2 \times 2 \times 2$ super-cell as obtained after full structural relaxations for any lithium composition from $x = 3$ to $x = 7$. For the sake of clarity, lithium atoms are not represented.

$Li_{11}MPn_4$ than for the relaxed Li_9MPn_4. This will be discussed in the next section. High-lithiated phases thus correspond to cubic lattices in which Pn atoms move back to their initial fcc crystallographic positions. Meanwhile, the $(MPn_4)^{x-}$ electron density becomes more diffuse to efficiently screen the numerous Li^+-Li^+ interactions induced by the addition of lithium. As shown by the contour plots in Figure 8c, $(MPn_4)^{11-}$ electron density is now strongly polarized around Pn atoms (spherical distribution), rather than along the M−Pn bonds when $x \leq 7$. Pnictogen atoms belonging to neighboring tetrahedra are now connected to each other. This is in agreement with XRD patterns collected for high-lithiated phases, reflecting a network of Pn anions with an fcc packing.

4. Theoretical/Experimental Confrontation and Mechanisms

The present experimental and theoretical study demonstrates equivalent structural, electrochemical, and electronic behaviors for every Li_xMPn_4 (MPn = TiP, VP, VAs) compound for $x = 3-11$. Theoretical calculations and structural relaxations confirm that Li_xMPn_4 phases behave as networks of nearly isolated $(MPn_4)^{x-}$ anions stabilized by xLi^+, as previously suggested. [18] These tetrahedral electronic entities have been shown to absorb large charge variations, thanks to the strong ability of their electron density to distort along M−Pn bonds. They accommodate slight contraction/expansion to compensate the lack/addition of lithium. This (MPn_4) "breathing" results in a loss/reconstruction of the unit cell fcc symmetry. The key point is that every structure from $x = 3$ to $x = 11$ exhibit equivalent long-range cubic order (statistical distribution) as well as equivalent local environment (MPn_4 tetrahedra) for the transition metal. The question about concern is the agreement between these results and in situ XRD patterns showing a reversible crystalline to amorphous phase transition upon charge and discharge. Actually, an XRD simulation of the low-lithiated phases reveals that the most intense peak of such cubic structures is ascribed to (200) planes, at a Bragg angle $2\theta = 30.0° \pm 1°$ (Cu $K\alpha_1$) for unit cell parameters $a = 6.0 \pm 0.2$ Å. Now, as shown in Figure 5, this specific peak also exists in the starting electrode XRD patterns ($Fm\bar{3}m$), but is one of the less intense peaks. This means that the metallic contribution to the total electron density is small and may explain why such a metallic (statistical) order could not be detected by X-ray. Low-lithiated and high-lithiated phases are thus structurally close, although their X-ray patterns strongly differ.

Of particular concern for electrode material application is the small volume variation associated with this structural mechanism. From $x = 3$ to $x = 11$, most of the structural change is achieved by the M−Pn bonds, while the unit cell volume is constrained by Li^+-Li^+ repulsions to undergo smaller variations ($\Delta a/a$ less than 5% from $x = 3$ to $x = 11$). It should be noticed here that both M−Pn bond lengths and volume changes are overestimated by single-cell type calculations since, in this model, each of the four Pn atoms cannot be connected to more than one transition metal. In real crystal, the statistical distribution of M over the 8-folded tetrahedral sites allows local situations in which Pn atoms are connected to more than one transition metal. In such situations, the M−Pn bond contraction is expected to be smaller, leading to averaged M−Pn bond lengths slightly greater than the reported values (Table 2). This is confirmed by $2 \times 2 \times 2$ super-cells relaxations in which M is statistically distributed over its eight positions and may explain why a better agreement with experiments is obtained for $Li_{11}MPn_4$ phases compared to that for Li_9MPn_4.

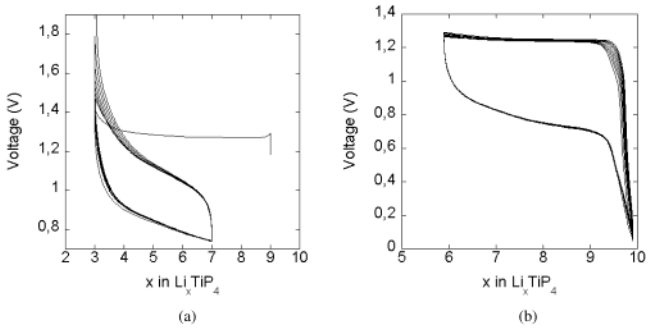

Figure 10. Voltage vs composition curves for Li_9TiP_4/Li cell for the first 20 cycles, with lithium composition manually set between (a) $3 \leq x \leq 7$ and (b) $6 \leq x \leq 10$. Both experiments have been started in oxidation from the Li_9TiP_4 lithium composition.

The two-phase process observed upon charge thus corresponds to a solid-state crystalline phase transition between a Pn-ordered phase (fcc) and a Pn-disordered phase (X-ray amorphous). Starting and charged electrodes showing equivalent cubic frameworks associated with close volumes, the phase transition should be easily reversed. This is consistent with the nearly complete fcc reconstruction (Figures 5a,b and 6), but not with the different charge and discharge potential shapes (Figure 2). Actually, entropy and kinetic barriers may be responsible for this. According to Li_7VPn_4 (Pn = P, As)[18] and Li_8TiP_4 electronic structures, two different electronic regimes have been associated with the fcc symmetry loss and reconstruction: fcc loss (respectively reconstruction) is achieved as far as electron transfers involve the low-lying band (respectively high-lying band). It is likely that the structural phase transition occurring in oxidation comes along a gain in entropy, thanks to the formation of a less symmetric low-lithiated phase in which Li^+ ions are probably disordered. The formation of Li_xMPn_4 ($3 < x < 9$) intermediate compositions should be hindered by the large kinetics barriers associated with Li^+ extraction from the high-lithiated starting electrode. In reduction, these kinetic barriers are obviously lowered since a large charge vacancy exists between every contracted $(MPn_4)^{x-}$. The two first processes observed upon discharge should thus correspond to a progressive Li^+ reinsertion into the low-lithiated electrode, to form intermediate Li_xMPn_4 compositions. From an electronic point of view, these processes occur until the complete filling of the low-lying band (i.e., up to $x_c = 7$ for Li_xVPn_4 and $x_c = 8$ for Li_xTiP_4). This corresponds to the first electronic regime for which no fcc reconstruction can occur. Note that a cationic ordering is probably responsible for the existence of two different processes during this part of the discharge, as already suggested by a previous analysis of Li^+-Li^+ electrostatic interactions in Li_xVPn_4 (Pn =

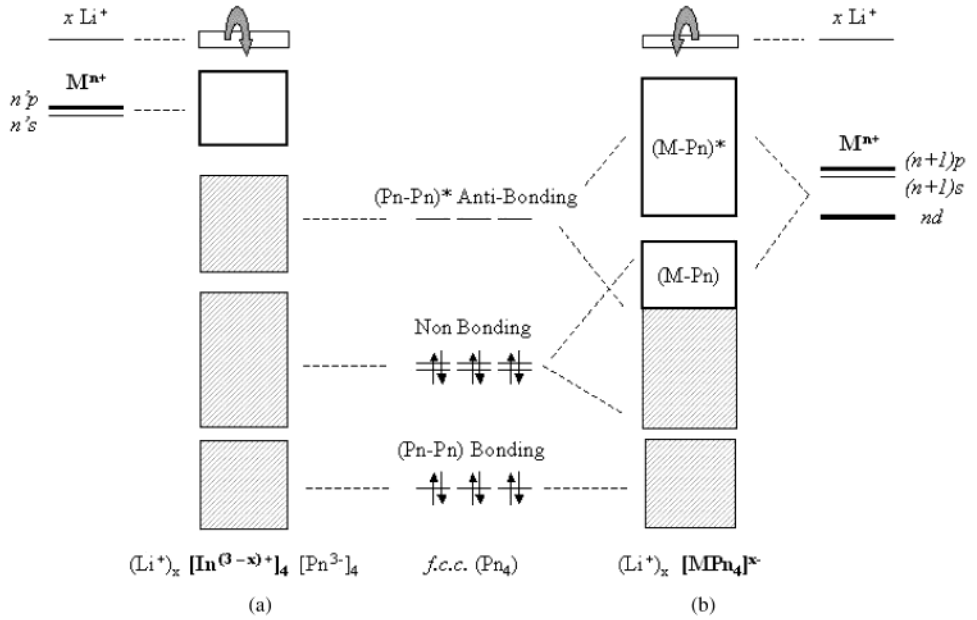

Figure 11. Qualitative electronic band structures for (a) InSb and (b) Li_7MPn_4 built from Pn_4 symmetrized molecular levels and M/Li atomic levels.

P, As). [18] Once the critical x_c composition is achieved, another process takes place to complete the discharge. This latter process is associated with the second electronic regime, for which an fcc reconstruction can occur. The reverse structural phase transition from a Pn-disordered phase to a Pn-ordered phase is thus achieved between x_c and the end of discharge.

To provide experimental evidence for this unusual mechanism, galvanostatic measurements have been carried out on Li_9TiP_4/Li cells for 20 sweeps of charge and discharge and in two different lithium composition intervals. First, the discharge was set to stop at $x = 7$ while a full charge was achieved (see Figure 10a). Second, the charge was set to stop at $x = 6$ while a full discharge was achieved (see Figure 10b). As clearly demonstrated by the resulting potential/composition curves, a lithium composition greater than x_c is required to allow the fcc reconstruction. Indeed, the two-phase plateau observed during the first charge of Li_9TiP_4 is replaced by a single-phase process in the next 10 charges, when discharges are stopped at $x_c = 7$ (Figure 10a). In contrast, the two-phase plateau is fully recovered while complete discharges are achieved (Figure 10b).

Concluding Remarks

The promising electrochemical activity of Li_xMPn_4 (MPn = TiP, VP, VAs) ternary phases toward lithium have been rationalized in terms of a reversible structural phase transition involving small electrode volume changes. The transition originates from a "breathing" of the $(MPn_4)^{x-}$ electronic entities that the initial fcc Li_9MPn_4 networks are based on. This leads to a loss/reconstruction of the fcc symmetry upon charge/discharge. The two phases involved in the oxidation process correspond to nearly size-equivalent cubic structures in which Pn are ordered (Li-rich) and disordered (Li-poor). The different kinetic barriers associated with Li^+ extraction from Pn-ordered electrodes and Li^+ insertion in Pn-disordered phases induce different mechanisms upon charge and discharge. The delayed fcc reconstruction shown by in situ XRD has been correlated to the occurrence of two different electronic regimes in Li_xMPn_4 electronic structures. Before the fcc reconstruction, the two different processes shown by potentiodynamic measurements have been correlated to two different ionic regimes, within the first electronic regime. Eventually, an equivalent cubic framework shared by both low-lithiated and high-lithiated electrodes has been invoked to explain the good reversibility of the structural phase transition.

The present study strongly suggests that fcc networks exhibit most of the crystallographic and electronic features required for competitive electrode materials. First, Pn-fcc unit cells provide a large number of cationic vacancies together with a large unit cell volume. Second, their electronic structure provides a large band of nearly Pn−Pn nonbonding levels. Provided that this band is involved in electrochemical redox processes, host material structural change should therefore be prevented. As illustrated in Figure 11, the implication of this specific band is directly correlated to the use of a transition metal. In contrast to InSb, [10] the formation of covalent M−Pn bonds in Li_7VPn_4 and Li_8TiP_4 bulks results in a strong M(3d)−Pn(np) hybridization, and therefore in an incomplete filling of the Pn-fcc nonbonding bands. Consequently, redox chemistry involves weakly interacting $(MPn_4)^{x-}$ anions in Li_xMPn_4 while it involves In^{n+} cations in Li_xInSb. This may explain the very different mechanism proposed by Thackeray and co-workers for InSb, that is, the extrusion of In^0 small particles when more than two Li^+ are inserted in InSb. [8] On another hand, it helps to better understand the results reported by other groups for Li_7MnN_4[20,21] and Li_7MnP_4. [22] Owing to the strong electronegative character of nitrogen, less covalent M−N bonds are expected compared to M−Pn (Pn = P, As). This results in an electron density mainly polarized outside the tetrahedral (MN_4) coordination sphere, that is, on the faces of the cubic unit cell, even for low lithium compositions.

The potential cages hence created on fcc faces likely disfavor Li^+ diffusion and/or large insertion number. One may now wonder whether Li_7MnP_4 behaves as every other Li_7MPn_4 (M = V, Ti). Actually, the first galvanostatic cycle provided by Nazar et al. in ref. 22 is fully consistent with the mechanism we propose. The rather large capacity loss observed at the end of charge, that is, after a complete Li^+ insertion in MnP_4 (monoclinic) to form Li_7MnP_4 (fcc), could be correlated to the reaction $Li_7MnP_4 - xLi \rightarrow [(x-4)/3]MnP_4 + [(7-x)/3]Li_3MnP_4$. An incomplete MnP_4 reconstruction would therefore be achieved upon charge, together with the formation of an X-ray amorphous Li_3MnP_4 phase. This is fully consistent with the ex situ XRD patterns carried out at the end of charge.[22] Note that the transition metal chemical nature is also responsible for the different behavior of Li_7MnP_4 compared to other transition metal-based pnictides. First, owing to the manganese electronic configuration compared to that of titanium and vanadium, this lithium composition leads to a partial filling of the high-lying band for every Li_7MnPn_4 (Pn = N, P, As) electronic structure. This may explain why fcc Li_7MnN_4 and Li_7MnP_4 exist for lower lithium compositions compared to those of vanadium ($x > 7$) and titanium ($x > 8$) pnictides. Second, MnP_4 exists while TiP_4 and VAs_4 are not stable structures.

CM035101L